ACS APPLIED MATERIALS & INTERFACES

www.acsami.org Research Article

Active Periodic Magnetic Nanostructures with High Aspect Ratio and Ultrahigh Pillar Density

Zhiren Luo, Xu A. Zhang, Benjamin Aaron Evans, and Chih-Hao Chang*

Cite This: *ACS Appl. Mater. Interfaces* 2020, 12, 11135−11143 Read Online

ACCESS | Metrics & More | Article Recommendations | Supporting Information

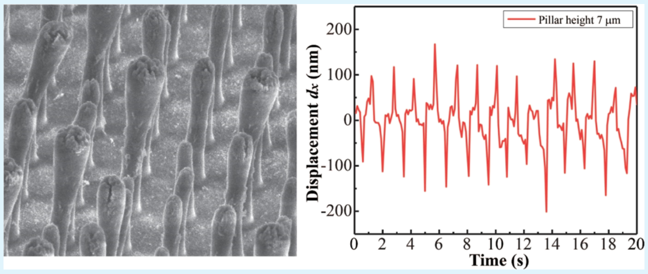

ABSTRACT: Magnetically actuated micro/nanoscale pillars have attracted significant research interest recently because of their dynamic properties. These structures can be used for various applications, such as dry adhesion, cell manipulation, and sensors or actuators in microfluidics. Magnetically actuated structures can be fabricated by mixing magnetic particles and polymers to yield a favorable combination of magnetic permeability and mechanical compliance. However, the pillar density of demonstrated structures is relatively low, which limits the potential applications in active surface manipulation of microscale objects. Here, we demonstrate active periodic nanostructures with a pillar density of 0.25 pillar/μm^2, which is the highest density for magnetically actuated pillars so far. Having a structure period of 2 μm, diameter of 600 nm, and high aspect ratio of up to 11, this structure can be magnetically actuated with a displacement of up to 200 nm. The behaviors of the pillars under various cyclic actuation modes have been characterized, demonstrating that the actuation can be well controlled. This work can find potential applications in particle manipulation and tunable photonic elements.

KEYWORDS: *dynamic materials, active nanostructures, nanofabrication, magnetic nanoparticles, high aspect ratio*

INTRODUCTION

In nature, micro/nanostructures resembling pillars that can be actuated are commonly observed and have many applications.[1−4] For example, the immotile primary cilia in human bodies can serve as sensors for smell, sight, and diseases.[1] The setae on gecko feet consist of hierarchical micro/nanopillars,[2] which enhances dry adhesion using van der Waals forces. Motile cilia are widely seen as actuators, such as those found in human lungs for mucociliary clearance and on corals for shielding fouling organisms.[3,4] Inspired by these structures, various research groups have engineered synthetic tunable micro/nanopillars for particle manipulation,[3] dry adhesion,[5−7] microfluidic actuation,[8−15] controllable wettability and fog harvesting,[16−22] anti-icing coating,[22] and tunable optical reflection or transmission.[23−25]

There are several actuation strategies to manipulate these micro/nanopillars in real time, such as temperature,[6,7,26−28] pH,[4,8,28] electric field,[4,9] and magnetic field.[3−5,10−25] A number of soft materials can be used for temperature-actuated dynamic micropillars. These include shape memory polymers with a thermoplastic effect,[6,7,27] hydrogels that can be mechanically stretched or contracted by temperature,[28] and liquid crystals that can change orientations to induce dimension changes.[6] However, the response time of temperature actuation can be slow and is generally on the order of minutes.[6,27,28] Hydrogels can also respond to pH to change the ionization degree and the osmotic pressure, therefore swelling or contracting to bend micropillars.[8,28] However, this requires distinct chemical environments, which might damage other materials. Electric field can also be used to induce mechanical[9] or pH/ion density variation for actuation.[4] However, this approach requires the use of saline solutions in the electrodes, resulting in a potentially corrosive environment. In addition, a power supply is needed and energy consumption needs to be considered.

Magnetic actuation has attracted attention as a viable strategy due to its short response time, reversible actuation, low energy consumption, high repeatability, and noncontact, nondestructive control.[10−24] To obtain a favorable combination of high magnetic permeability and low mechanical stiffness, many magnetically actuated structures consist of soft polymer as a matrix with an embedded magnetic material. Such a strategy has been implemented using different magnetic materials, such as NdFeB microparticles,[5] iron oxide nanoparticles,[10,11,25] cobalt nanowires,[12] cobalt microparticles,[19] and carbonyl iron particles.[14,20−23] These magnetic structures demonstrate dynamic behaviors under magnetic actuations. However, they are mostly at the micron scale and have relatively low pillar densities. It should be noted that feature

Received: October 10, 2019
Accepted: February 4, 2020
Published: February 4, 2020

https://dx.doi.org/10.1021/acsami.9b18423

sizes of pillars including diameters and periods in this work are described as pillar densities ρ for convenience, which are defined as the number of pillars over unit area. As the pillar densities become higher, the feature sizes become smaller, potentially enabling the manipulation of smaller length scale objects such as particulates, cells, and visible light. Besides, it is important to get as small feature as possible so that the structure behaves more like a continuous material. High aspect ratio (AR) is also desirable because it has high compliance and can generally improve the actuation range.

However, there are still challenges in fabricating magnetically actuated structures with high pillar density and high AR. First, forces due to magnetic field gradients drop dramatically as the length scale decreases, resulting in reduced movement at small length scales.[5,14,29] Second, while torques due to uniform magnetic fields may dominate at small length scales, they require high-AR structures, which are mechanically weak and tend to collapse.[10,29] Third, magnetic microparticles or nanowires have high saturation magnetization, which is helpful for actuation but hinders the reduction of feature size to submicrometer scale.[12,17−21] Finally, patterning and fabrication processes may limit the pillar density and AR of periodic structures.[10,11,30,31] Soft lithography limits the AR because the mechanical force can induce structure collapse during the peeling process, and wet etching can also cause lateral collapse because the surface tension of solvent can pull pillars together during drying. Varying surface tension with sonication and critical point drying could be a solution, but it is difficult to entirely eliminate collapse. In addition, the high surface energy magnetic particles and functional chemical segments in the replica, such as iron oxides and amino groups, tend to increase adhesion to the mold and make fabrication even more difficult.

Many existing magnetic structures are fabricated by soft lithography with low pillar densities of 10^{-6} to 10^{-2} pillar/μm^2, corresponding to periods of 10−1000 μm.[12,19] The AR is also limited, with values typically below 9. High-AR nanostructures have been fabricated using molds that can be chemically dissolved;[10,11] however, these pillars are randomly distributed with low pillar density around 0.02 pillar/μm^2. Periodic nanopillar arrays with high pillar density of 0.25 pillar/μm^2 or period of 2 μm have been generated; however, the AR of these structures is around 1.[25] Magnetic micropillars can be fabricated by linking magnetic nanospheres to high-AR chains, but the pillar geometry varies largely.[15] Magnetically actuated pillars can also be generated by other methods, such as electrodeposition and maskless fabrication by magnetic field. However, these structures tend to have low pillar densities of 10^{-7} to 10^{-3} pillar/μm^2 and have large deviation in pillar geometry.[21,22,24] A summary of the materials and geometries of these structures is discussed further in Supporting Information Section A and plotted in Figure 1. Here, the pillar density is plotted versus AR, with the desirable region being in the upper right corner. It can be noted that there is a competition between the density and AR of the magnetic nanostructures, and it is difficult for them to be simultaneously obtained. Therefore, the study of structures with both high pillar density and high AR has yet to be explored.

In this work, we report a strategy to fabricate magnetically actuated nanopillar arrays with ultrahigh pillar density and high AR. This method introduces a sacrificial mold into the replication process which can be removed using reactive ion etching (RIE). Nanopillar arrays with a period of 2 μm have been demonstrated, where the pillar has a 600 nm diameter and 7.7 μm height. This yields a pillar density of 0.25 pillar/μm^2 and AR up to 11, as shown in Figure 1. This pillar density is the highest yet demonstrated, which is at least 10 times higher than those reported in the literature. Simultaneously, the AR in this work is among the highest ARs reported. This work also reveals the possibility of combining high pillar density and high AR in magnetic nanostructures. Experimental characterization demonstrates that the nanopillar can be tilted with a pillar top displacement using permanent magnets. Other cyclic actuation configurations are also examined to further demonstrate oscillating and sweeping motions. In addition, the fabricated magnetic nanopillars have been tested for particle manipulation. Because the feature size of each pillar is in the order of 100 nm, the periodic nanopillar array could have more potential applications such as the dynamic tuning of visible light and the manipulation of microscale particulates.

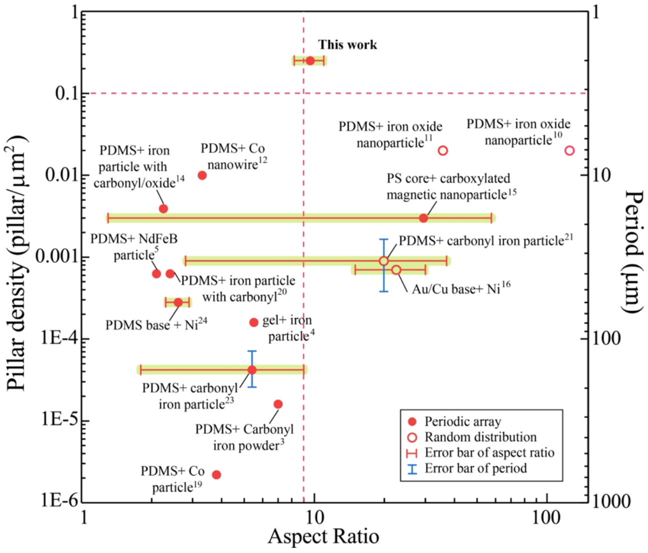

Figure 1. Comparison of pillar density and AR of magnetically tunable pillars from literature. The bars represent the range of AR or pillar density.

■ EXPERIMENTAL APPROACH

The fabrication process for the magnetic nanopillar array is illustrated in Figure 2. Initially, a water-soluble poly(4-styrenesulfonic acid) (PSS) layer with 160 nm thickness, anti-reflection coating (ARC) with 100 nm thickness, and negative photoresist SU-8 with 10 μm thickness are spincoated on silicon substrates, as shown in Figure 2a. Then 2D periodic hole array is patterned in the photoresist layer using Lloyd's mirror interference lithography with a 325 nm laser.[32,33] The depth of the holes is controlled by the photoresist thickness and exposure dose and is designed to be as deep as possible. The subsequent replication process uses a magnetic material ferrofluid-polydimethylsiloxane (FFPDMS), which is composed of iron oxide nanoparticles (Fe_3O_4, diameter of 7−10 nm) uniformly and permanently bonded into a matrix of aminopropylmethylsiloxane-*co*-polydimethylsiloxane (APMS-*co*-PDMS) copolymer.[10,34] This material is superparamagnetic due to the small particle size, and the saturation magnetization is 12.98 A m^2/kg for FFPDMS with 25 wt % iron oxide. Consisting of 75 wt % polymer, it is also mechanically compliant, with a Young's modulus of 1.26 MPa.[34] During the replication process, the FFPDMS is applied to the SU-8 mold and cured using formaldehyde vapor, resulting in high-AR nanopillar replica, as shown in Figure 2b. Then, the whole structure is transferred onto a glass substrate and separated by dissolving the PSS layer in deionized water, as shown in Figure 2c. More details of the replication and transferring process are discussed in Supporting

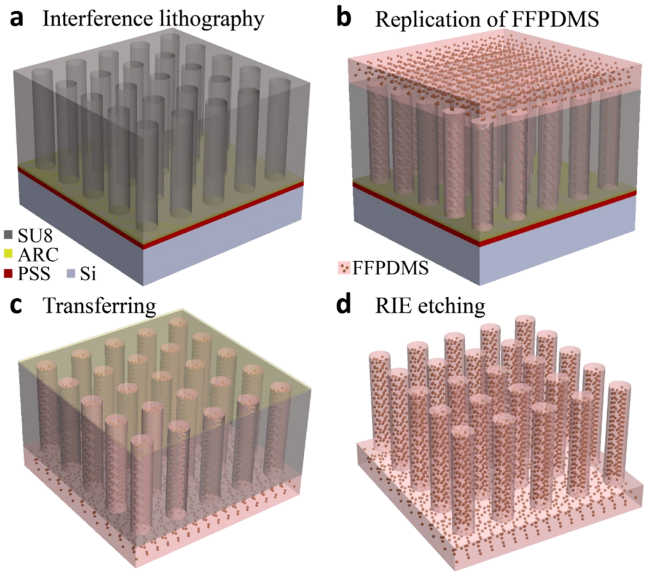

Figure 2. Fabrication processes of magnetic nanopillar array. (a) Photoresist is patterned using interference lithography to generate an array of holes. (b) FFPDMS is applied into the photoresist mold during the replication process. (c) structure is transferred onto a glass substrate by dissolving the PSS layer. (d) ARC and photoresist layers are removed using RIE process.

Information Section B. After the transferring process, the ARC layer and photoresist mold are removed by O_2 and CF_4 RIE, leading to an exposed high-AR FFPDMS nanopillar array, as shown in Figure 2d. During the whole fabrication process, the high-AR nanopillars are stable without collapse because the SU-8 mold protects the nanopillars during the transferring. In addition, RIE does not induce collapse due to the dry etching environment.

The scanning electronic microscopy (SEM) images of the SU-8 mold and the fabricated FFPDMS nanopillar array are depicted in Figure 3. The structures have a square lattice and consist of holes with period of 2 μm, as shown in Figure 3a,b. The average depth of the holes is around 6.4 μm and can range from 5.9 to 6.9 μm. Note that the thickness of the SU-8 layer is 10 μm; thus, the hole does not extend completely through the thickness of the mold. In addition, the hole geometry is not uniform. These shorter and nonuniform holes can be attributed to the relatively thick SU-8 layer and the short wavelength of the ultraviolet (UV) light source. The SU-8 absorbs the light efficiently at short wavelength below 365 nm ("i-line").[35] With the 325 nm UV light source, the light intensity drops gradually along the light penetration direction across the thickness of the SU-8. Therefore, the depth and diameter of the holes array are sensitive to the exposure dosage and the depth can be controlled from 0.2 to 6.9 μm, as discussed in Supporting Information Section C. Note that because the resist layer absorbs and scatters the UV light, the exposure latitude is narrow and small variations in processing can contribute to nonuniformity in hole geometry and the replicated nanopillars.

The SEM images of the fabricated FFPDMS pillar array after mold removal are shown in Figure 3c,f. The pillars are relatively uniform over the pattern area of 7 mm × 9 mm. The average AR in Figure 3c,d is around 8.2, and the maximum AR is around 11 for pillars with 7.7 μm height and 700 nm diameter. The pillars at another position within the same sample are comparatively more uniform as shown in Figure 3e,f, where the average AR is around 9.0 for pillars with 6 μm height and 670 nm diameter. Note the top diameters of pillars in Figure 3c tend to be larger than the bottom. For example, the bottom diameter of the tallest pillar in Figure 3c is 700 nm while the top diameter is 1.6 μm. This nonuniform pillar shape can be attributed to the top part of SU-8 receiving a higher dose than the bottom part, leading to a larger hole diameter at bottom and a smaller diameter at top, as discussed in Supporting Information Section C. This is consistent with the well-known profiles with negative sidewall angles for thick SU-8 structures.[35] The nonuniform shape is helpful for actuation because the smaller diameter lowers the bending stiffness at the pillar base.

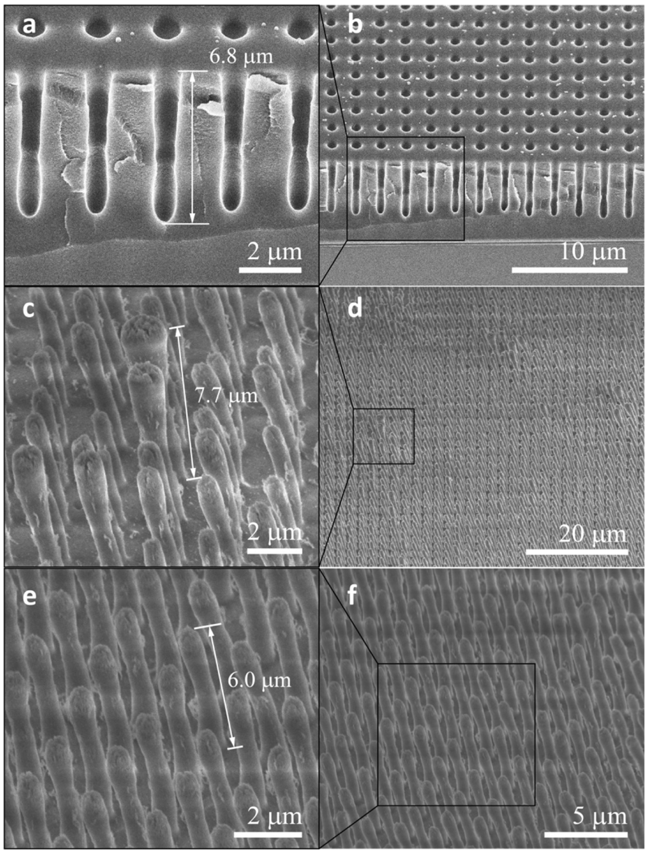

Figure 3. SEM images of fabricated SU-8 mold. (a,b) Cross-section view of the deep profile after exposure. (c) High- and (d) low-magnification side-views of the tallest pillar with height around 7.7 μm and AR of 11. (e) High- and (f) low-magnification of fabricated sample. The tallest pillar is around 6.0 μm high with an AR of 9.

RESULT AND DISCUSSION

To examine the tilting of the nanopillar array under translational actuation, the displacement of the pillar top is observed using optical microscopy. In this experiment, a cylindrical FeNdB permanent magnet with a 2.54 cm diameter and 4 cm length is translated in the in-plane direction beneath the substrate, as illustrated in Figure 4a. The pillar array is roughly 2 mm away from the magnet face and experiences a magnetic flux density of 0.5 T. The distance between the centerline of magnet and the structure is defined as x_m, which is relative to the field direction on the structure. More details regarding the testing configuration are discussed in Supporting Information Section D. The nanopillars are induced to tilt, and consequently, the pillar tops move toward the left and right, as shown in Movie 1. This movie is recorded by a camera under an optical microscope with 1000× magnification. It is noted that the taller pillars with larger top diameters move more than the shorter pillars, which generally have smaller diameters. To demonstrate the movement better, individual frames at 0.1 s intervals are extracted from Movie 1 and illustrated in Figure 4b,d. When the magnet is directly beneath the substrate (x_m = 0 cm), there is a vertical magnetic field through the pillar array.

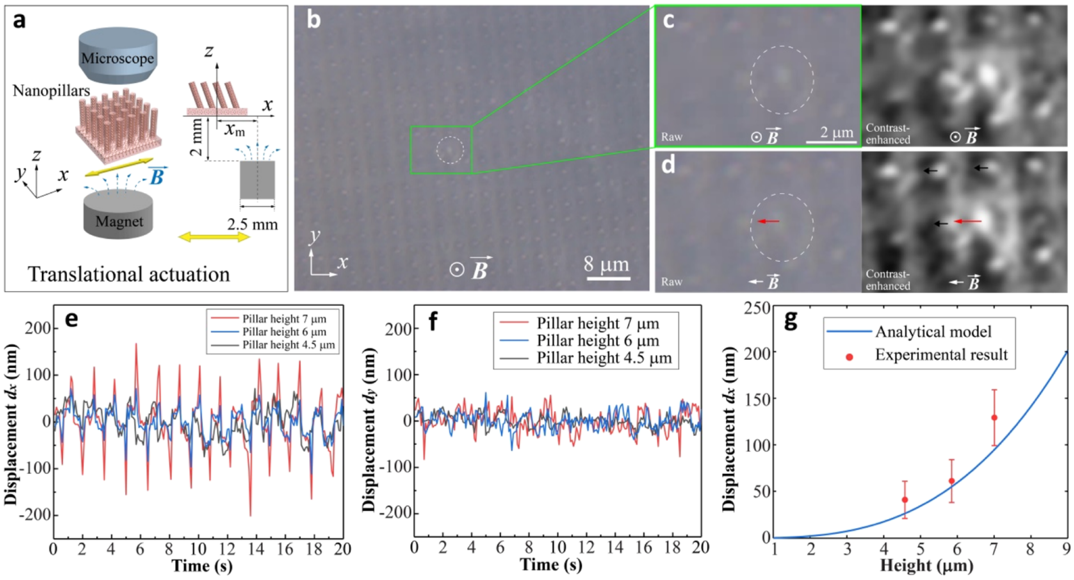

Figure 4. Displacements under the translational actuation. (a) Schematic of the actuation setup. (b) Top-view microscope image focusing on the top of nanopillars when there is vertical magnetic field. (c) Higher magnification image of (b) and its responding contrast-enhanced image. (d) Higher magnificent image and its responding contrast-enhanced image when the magnetic field is pointing toward the negative *x* direction. (e) Displacement versus time in *x* direction d_x of pillar top with different pillar heights. (f) Displacement versus time in *y* direction d_y of pillar top. (g) Relationship between pillar height and d_x based on analytical model and experimental results. The error bars are based on the standard deviation of the peak displacements.

Pillars do not tilt and the dashed white circle represents the initial position of a tall pillar, as shown in Figure 4b,c. When the magnet is located with about 1 cm along the positive *x* direction (x_m = 1 cm), the magnetic field at nanopillars is tilted from vertical toward the negative *x* direction at a 45° angle. Consequently, pillars are tilted toward the negative *x* direction. The red arrow indicates the pillar top shifts to the left in Figure 4d. This shift in *x* direction can be defined as the displacement d_x, which is around −200 nm. Here, the minus sign means that the displacement is toward the negative *x* direction. The black arrows show the displacements of the surrounding pillars which move at the same frequency as the tall pillar.

The quality of the raw microscope images in this work is relatively low because the structures are near the optical diffraction limit of the optical microscope. In addition, the imaging needs to be performed in reflection mode because the magnet would block the path of transmission. This would also reduce the image quality due to the absorption of FFPDMS, as discussed in previous work.[25] To better quantify the pillar displacement, image processing is used to analyze the raw microscope images extracted from the recorded videos. In this process, the original images are converted to grayscale and then the pixel saturation is increased, resulting in the contrast-enhanced images in Figure 4c,d. Note the displacement of the pillars can be observed more clearly in the contrast-enhanced images. The images are then convolved with a circle kernel to determine the pillar centroids, which can be used to calculate the displacements. Note that this process assumes that the degree of blur and shape of the pillar do not change during actuation. This allows the relative displacement tracking of pillar centroids with the subpixel resolution, which is consistent with the imaging methods commonly used in the cell testing on extracellular matrices.[36,37] More details about image processing are discussed in Supporting Information Section E, which also includes the tracking of multiple pillars.

The image analysis algorithm is then used to analyze the displacements over time for different pillars with heights of 7, 6, and 4.5 μm, as shown in Figure 4e,f. Here, the displacements d_x are plotted versus time as the magnet is translated along the *x* direction, as shown in Figure 4e. This result demonstrates that the movement of pillar is repeatable over 15 cycles in time. In each cycle, the displacement d_x has a positive and negative peak corresponding to the actuation direction. The maximum displacements of short (4.5 μm height), medium (6 μm height), and tall (7 μm height) pillars are 69, 111, and 200 nm, respectively, indicating that the tilting of the nanopillar increases when the height increases. This is consistent with the movement of pillars in Movie 1. Compared with d_x, the displacements in the *y* direction d_y are random and close to zero over time because there is less variation in the magnetic field in the *y* direction, as shown in Figure 4f. The measurement error and noise level of the characterization system is around 5 nm, which is measured using a nonmagnetic polydimethylsiloxane (PDMS) pillar array, as discussed in Supporting Information Section F. This indicates that the characterizing system itself does not induce any displacement during actuations to intervene in the result of FFPDMS pillars. The movement of PDMS is also shown in Movie 2, which is negligible.

To better investigate the tilting reflection behavior of nanopillars under magnetic actuation, a simple analytical model can be introduced. According to this model, the magnetic torque on the nanopillar is highest when the angle between magnetic field and nanopillar is 45°, which predicts the optimal orientation for the experiment mentioned above, as discussed in Supporting Information Section D. The tilting angle φ is expressed as $\varphi = \frac{\mu_0 M^2 \rho_m^{\ 2}}{E}\left(\frac{L}{D}\right)^2$ based on the balance of mechanical energy and magnetic energy, under the assumptions that the pillar cross section is uniform and the curvature is constant along the pillar height.[29] It is noted that because the pillars in this work are tall with AR around 10, it is reasonable to ignore any viscoelastic effect in the polymer.[38] Here, μ_0 is the vacuum magnetic permeability, $M = 9.5$ A m^2/kg is the magnetization at 0.5 T, $\rho_m = 1227$ kg/m^3 is the mass density, $E = 1.26$ MPa is Young's modulus. L is the pillar height, D is the pillar diameter, and L/D is the AR. The displacement d can be approximated as $d = \varphi L$ for small deflection, yielding

$$d = \frac{\mu_0 M^2 {\rho_m}^2}{E}\left(\frac{L}{D}\right)^2 L$$

This model indicates that high AR is critical and influences the actuation significantly because d is proportional to the square of AR and the cube of L. The analytical relationship between the displacement d and the pillar height L is plotted in Figure 4g along with the corresponding experimental results. Here, the red dots represent the measured average peak displacements and the error bars are the corresponding standard deviations. It can be observed that the experimental results roughly match with the analytical model. In particular, the experimental displacements are slightly larger than those in the analytical model because the cross section used in simulations is assumed to be constant along the pillar. However, the actual pillar geometry typically has larger diameter on the top and smaller diameter on the bottom, resulting in the underestimation of the pillar displacement in the model. The displacement in this model is induced by magnetic torque under uniform magnetic field as the dominant mechanism because the displacement component induced by magnetic force based on the field gradient is too small to be considered. More details of these two models are discussed in Supporting Information Section G, which also explains the challenges as previously mentioned.

Beyond manual translation of the magnet, which results in quasistatic actuations, the cyclic actuation of the nanopillars at low frequencies has also been characterized, as shown in Figure 5. In these experiments, the magnet is driven by a mechanical wave driver with frequencies from 1 to 4 Hz, leading to the oscillation of the nanopillar array. The displacement of the magnet is around 2 cm. At an actuation frequency of 4 Hz, the nanopillar is driven to oscillate quickly as shown in Movie 3. The displacements of the pillar tops in the time domain are extracted from the video and plotted in Figure 5a. The frequency spectrum of the signal is then calculated using fast Fourier transform (FFT), as shown in Figure 5b. Here, it can be observed that the spectrum has a peak at 4 Hz, demonstrating that the pillar displacement is at the same speed as the corresponding actuation frequency. Similarly, when the actuation frequency decreases to 2 Hz, the nanopillars oscillate more slowly, as shown in Movie 4. The extracted pillar displacements are plotted versus time in Figure 5c, with the corresponding FFT spectrum containing a peak at 2 Hz, as shown in Figure 5d. When the actuation frequency is further reduced to 1 Hz, as shown in Movie 5, the pillar swings even slower. The extracted pillar displacements versus time are plotted in Figure 5e, and the corresponding frequency spectrum has a peak at 1 Hz, as shown in Figure 5f. It can be noted that the absolute displacement decreases as the frequency increases from 1 to 4 Hz, because the vibration amplitude of the wave driver drops as the frequency increases. Faster actuation and the role of fatigue will be tested in the future. Because the natural resonant frequency of the nanopillar is around 61.3 kHz as discussed in Supporting Information Section H, high-frequency actuation could be used to induce larger pillar displacement at resonance.

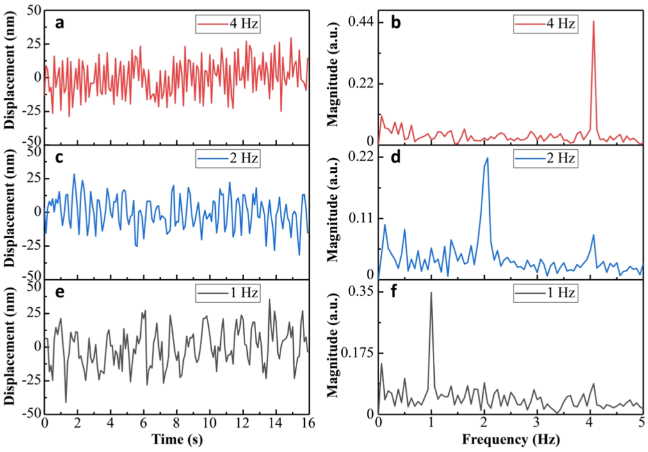

Figure 5. Response of nanopillars under cyclic actuations. The displacements over time with actuation frequencies of (a) 4, (c) 2, and (e) 1 Hz. The corresponding frequency spectra calculated using FFT indicate peak frequencies at (b) 4, (d) 2, and (f) 1 Hz, agreeing with the actuation frequencies.

The results under cyclic actuations are taken by a camera with a frame rate of 10 frames/s, and no obvious lag between the displacement and actuation has been observed, which demonstrates the pillar array has fast response and high repeatability. This can be due to the superparamagnetism of FFPDMS. There is no actuation hysteresis in the FFPDMS nanopillar, which would be magnetized immediately along the external field direction once the field is applied. When the external field changes direction, the magnetization will change to align with the external field direction easily and induce movement. If the external magnetic field is removed, there will be no residual field remaining in FFPDMS. In addition, the mechanical tilting of the nanopillar is in the elastic deformation regime because the polymeric matrix is soft, the AR is high, and the internal strain is small. Therefore no residual strain remains when the actuation torque is removed, resulting in the fast response and high repeatability as well.

The pillar responses under rotational actuation are also characterized, where the magnet is rotated in the clockwise and counter-clockwise directions, as illustrated in Figure 6a. The magnet is 1 cm off-center and 8 mm under the nanopillars. In this actuation mode, the nanopillars rotate with the magnetic field resembling a sweeping motion, as shown in the inset of side view in Figure 6a. Here, the pillar top rotates along a circular path as indicated by the dashed circle in the inset diagram. During the rotation, the displacement components d_x and d_y versus time can be regarded as sinusoidal wave functions with their own amplitudes and phases. It can be predicted that the amplitudes of d_x and d_y are similar, while the phases should have a constant offset $\Delta\phi = \phi_x - \phi_y$. In the clockwise rotation, d_x reaches positive peaks later than d_y, resulting in a phase lag of $\Delta\phi = -90°$, as shown in the inset diagram in Figure 6a. In contrast, the counter-clockwise rotation results in a phase lead of $\Delta\phi = 90°$.

The experimental movements of nanopillars under rotational actuations at 1 Hz are illustrated in Movie 6. The nanopillars are actuated to rotate clockwise in first 10 s and then counter-clockwise in the latter 10 s, demonstrating the isotropy of the

https://dx.doi.org/10.1021/acsami.9b18423
ACS Appl. Mater. Interfaces 2020, 12, 11135−11143

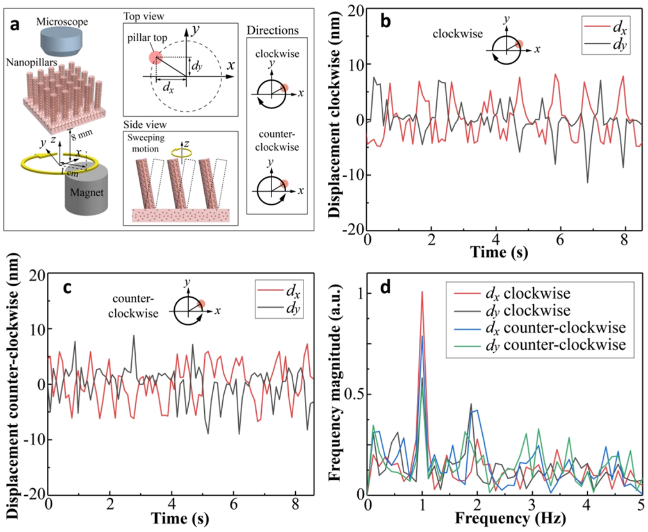

Figure 6. Nanopillar response for rotational actuation. (a) Schematic of the rotation actuation setup. (b) Displacements d_x and d_y vs time for clockwise actuation. It indicates that d_x lags behind d_y. (c) Displacements d_x and d_y vs time for counter-clockwise actuation. It indicates that d_x leads d_y. (d) Frequency spectra of d_x and d_y for both clockwise and counter-clockwise rotational actuations.

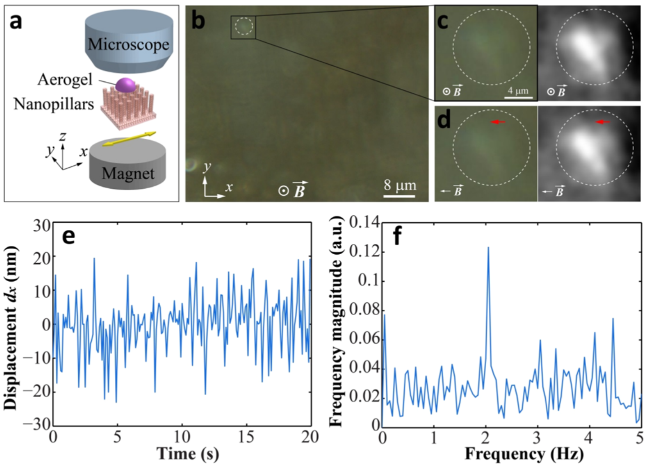

Figure 7. Particle manipulation of silica aerogel particles. (a) Schematic of the setup for the particle manipulation test. (b) Top-view microscope images of the particle under a vertical magnetic field. (c) Higher magnification image of (b) and its corresponding contrast-enhanced image. (d) Higher magnification image and its corresponding contrast-enhanced image when the magnetic field is pointing toward the positive x direction. (e) Displacement d_x of the particle over time. (f) Frequency spectrum of the d_x signal.

tilting toward any direction in $x-y$ plane. The displacements in the clockwise rotation are extracted from Movie 6 and plotted in Figure 6b, leading to roughly equivalent amplitudes and a phase lag for d_x and d_y, as expected. On the other hand, the displacements in the counter-clockwise rotation are plotted in Figure 6c, which validates the prediction of similar amplitudes and a phase lead. To further analyze the displacement curves, their frequency spectra are calculated using FFT and plotted in Figure 6d. The spectra for the d_x and d_y signals in both clockwise and counter-clockwise rotational actuations have peaks at 1 Hz, consistent with the actuation frequency. The phase shifts $\Delta\phi$ in Figure 6b,c are calculated using FFT as well. More details can be found in Supporting Information Section I. The results show that the phase lag in the clockwise rotation is approximately $\Delta\phi = -54°$, and the phase lead is approximately $\Delta\phi = 106°$ in the counter-clockwise rotation, which roughly match with the ideal situations with deviations of 16−36°. This may be due to the rotation being elliptical instead of perfectly circular and the magnetic flux density as a function of displacement is not linear. The deviations can also be attributed to the misalignment of the actuation, to signal noise, and to limited spectra resolution.

Because these nanopillar arrays can be actuated to oscillate and sweep with good control, they may find potential application as an active surface for microscale particulate contaminant manipulation. This is demonstrated by using 20 μm particles consisting of silica aerogel, which is very light with a bulk density of 30−100 kg/m^3. The aerogel is chemically stable, which can prevent the particles from reacting with nanopillars or being contaminated in air. The aerogel particles are also semitransparent, which facilitates the observation of FFPDMS nanopillars through aerogel particles using optical microscopy, such that the tops of the pillars can serve as references. In addition, the aerogel particle is nonmagnetic, which can that indicate the motion will be driven by the actuation of the nanopillars.

The aerogel particles are placed onto the FFPDMS nanopillars as shown in the schematic in Figure 7a. The nanopillars are then actuated to oscillate at a frequency of 2 Hz in the x direction using the previously described setup. Under this magnetic actuation, the aerogel particles also show movement in the x direction, as shown in Movie 7. The corresponding displacements of aerogel particle versus time are extracted and plotted in Figure 7b−d. With a vertical magnetic field at $x_m = 0$ cm, the aerogel particle begins at the initial position indicated by the dashed white ellipse shown in Figure 7b,c. When the magnet moves to the positive direction as $x_m > 0$ cm, the external magnetic field tilts toward the negative x direction, and the aerogel particle will move to the negative x direction as well, as indicated by the red arrow in Figure 7d. Further analysis of displacement is done using image processing and shown in Figure 7e. The displacement curve demonstrates the aerogel particle moves in periodic cycles with a maximum d_x of 20 nm. Note that the noise is relatively higher compared with previous measurements, which can be attributed to random movement of the particle due to environmental disturbances. The frequency spectrum of the aerogel particle displacement is calculated using FFT, as shown in Figure 7f. A peak can be observed at 2 Hz, which is consistent with the actuation frequency. The nanopillars can still be seen through the aerogel as an array of blurry circles in Movie 7, especially a tall pillar which is bright at left bottom corner. This nanopillar has maximum d_x of around 15 nm versus time and a peak of 2 Hz in frequency spectrum, verifying the actuation, as discussed in Supporting Information Section J. The aerogel particles can move in synchronization with nanopillars during the actuation and can be easily removed using nitrogen gun. This result indicates that the aerogel particles can be well manipulated by the FFPDMS nanopillar array in periodic motion with specific frequencies.

It can be observed that the pillar displacements are typically around 10−30 nm for the cyclic actuations which are much smaller than the displacement of the manual translational actuation. This can be attributed to the larger vertical distance to the sample, which is increased to 8 mm to avoid potential collision with the magnet because there is a vertical fluctuation from the mechanical system during cyclic actuations. As a result the magnetic field is reduced to 0.2 T, leading to a lower actuated displacement around 38 nm based on the analytical model, as discussed in Supporting Information Section D. Another limitation can be the smaller displacement of the magnet at higher frequency. This results in smaller changes in field direction and hence smaller actuated displacement as well. More details are discussed in Supporting Information Section D. In the future, the fluctuation needs to be reduced and the accuracy of the system needs to be improved to reduce the distance between the magnet and nanopillars, which would result in enhanced displacements.

While the fabricated magnetic nanopillar arrays have demonstrated successful actuation using a permanent magnet, the maximum demonstrated displacement of 200 nm is relatively small. This can be attributed to the limited AR of the pillar, currently at 8.2−11. Future work will focus on increasing the AR of the nanopillars to enhance the degree of actuation. According to the analytical model, the displacement of pillar top is proportional to the square of the AR. Therefore, doubling AR to 20 can increase the displacement 4-fold. This is achievable using the existing fabrication method, where thicker SU-8 layers of up to 20 μm can be considered. In addition, the pillar diameter can also be decreased to increase AR. This can be accomplished through lithography or post-exposure etching, which is currently being studied. However, for higher-AR nanopillars, more attention should be paid to avoid structure collapse during fabrication and testing because the structure is less mechanically stable.

The adjustment of material composition is another method to improve actuation. This includes controlling the concentration of iron oxide nanoparticles in FFPDMS, the Young's modulus of the polymer matrix, or even using other types of magnetic particles. Based on the analytical model, higher concentration of iron oxide nanoparticles can induce larger magnetization M, increasing displacement d. However, at higher concentration above 39 wt %, the Young's modulus E of the composite material will sharply increase as well to reduce compliance. There is an optimal concentration around 33 wt % for actuation, illustrated by the theoretical model and experiments in previous work.[34] Considering the fabrication difficulty, FFPDMS with lower iron oxide concentration is less viscous and can more readily fill the holes of the SU-8 molds, which facilitates the replication process. Therefore, 25 wt % concentration was chosen to prototype the high-AR periodic nanopillars in this work. Future work will investigate the effect of higher oxide concentration on FFPDMS pillar fabrication and actuation.

■ CONCLUSIONS

We demonstrate a high-AR and ultrahigh density periodic nanopillar array that can be magnetically actuated. The pillar density is 0.25 pillar/μm^2, which is among the highest densities reported for magnetically actuated pillars. The nanopillars have 600 nm diameters and heights up to 7.7 μm, yielding a high AR of 11. The fabricated nanopillar array can be tilted under magnetic actuation to have around 200 nm displacement, which agrees with the magnetic and mechanical models. The pillars can be actuated using cyclic actuation for an oscillation motion of 4 Hz, and possibly to higher frequencies given that no transient effect can be measured. The fabricated nanostructure also can be controlled under rotational actuation, resulting in a sweeping motion. This result is verified by the frequency spectra of the displacements and the phase offsets for both the clockwise and counter-clockwise directions. Beyond pillar actuation, the magnetic pillar array can be used to manipulate the movements of silica aerogel particles, demonstrating that the particle manipulation is potentially feasible for the nanopillar array. The high-AR magnetically actuated nanopillar array can also be potentially utilized for cell manipulation or as a material with dynamic optical properties.

■ METHODS

Fabrication of FFPDMS Nanopillar Array. The sample for the nanostructure mold consists of SU-8, ARC, and PSS. The PSS aqueous solution with 5 wt % concentration is spincoated onto the 500 μm-thick silicon substrate and baked on the hotplate at 185 °C for 5 min. Then, ARC i-CON-7 and SU-8 layer are spincoated and baked at 185 and 90 °C on hotplate for 1 min, respectively.

The photoresist sample is then exposed twice by orthogonal exposure using Lloyd's mirror interference lithography with 325 nm laser. A dose of 2 mJ/cm^2 is used for each exposure. During interference lithography, the ARC layer is used to reduce the reflection from the silicon substrate at the photoresist interface. Then, the sample is post-exposure-baked at 80 °C for 3 min, developed in propylene glycol methyl ether acetate solvent for 1 min, and rinsed with isopropyl alcohol for 1 min. As a result, the sample forms a 2D square pattern with deep circular holes, serving as the mold for the following replication process.

The FFPDMS is synthesized using iron oxide nanoparticles with a diameter of 7−10 nm, which are made from the reaction of ferric chloride and ferrous chloride salts in ammonium hydroxide solution. Then, this aqueous solution is mixed with a copolymer of APMS and DMS. The copolymer forms permanent bond with iron oxide nanoparticles using the amine group. The aqueous phase is then rinsed away, leaving behind uniform FFPDMS. The synthesized FFPDMS is poured on the SU-8 mold and cured using formaldehyde vapor. The cured FFPDMS is then separated from the substrate and transferred to a glass substrate by dissolving the PSS layer in deionized water. More details of the replication process and transferring process can be found in Supporting Information Section B.

The remaining SU-8 pattern and ARC layer are removed using O_2 RIE to form the FFPDMS nanopillar array. The structures are cleaned using CF_4 RIE to remove the potential oxide shells, which may form on the FFPDMS surface during the O_2 etching. For both etch processes the etching pressure is set as 150 mTorr and the RIE power is set to 250 W. The gas flow of O_2 is set as 80 sccm and the gas flow of CF_4 is set as 20 sccm. This process removes the ARC and SU-8 completely, resulting in the FFPDMS nanopillar array.

■ MATERIALS IN CHARACTERIZATIONS

The SEM images are taken by FEI Quanta 3D FEG. The top-view microscope images during actuation are taken by Leitz Wetzlar microscope with 1000× magnification. The image processing analyses are done by software ImageJ and Matlab. The oscillation is generated by mechanical wave driver Pasco Scientific SF-9324 and the function generator PASCO WA-9867 Sine Wave Generator. The magnet used in this work is a cylindrical permanent FeNdB magnet with a diameter of 25.4 mm and height of 40 mm. The magnetic field is experimentally measured by Guassmeter Model GM-2 (Alphalab Inc.) and simulated using software FEMM. The material used in particle manipulation test is aerogel JIOS AeroVa (D20 Grade) with a bulk density of 30−100 kg/m^3.

■ ASSOCIATED CONTENT

Supporting Information

The Supporting Information is available free of charge at https://pubs.acs.org/doi/10.1021/acsami.9b18423.

Additional information of comparison of engineering tunable pillars from different groups, fabrication details of high-AR FFPDMS nanopillars, trimming process during etching, phase difference calculation, and the calibration of particle manipulation test (PDF)

Movement of FFPDMS nanopillars under the translational actuation. This video is raw data without any image processing (MP4)

Movement of PDMS nanopillars under the translational actuation. This video is raw data without any image processing (MP4)

Response of FFPDMS nanopillars under cyclic actuations at 4 Hz. This video is raw data without any image processing (MP4)

Response of FFPDMS nanopillars under cyclic actuations at 2 Hz. This video is raw data without any image processing (MP4)

Response of FFPDMS nanopillars under cyclic actuations at 1 Hz. This video is raw data without any image processing (MP4)

Response of FFPDMS nanopillars under the 1 Hz rotational actuation. This video is raw data without any image processing (MP4)

Movement of silica aerogel particles under cyclic actuations at 2 Hz. This video is raw data without any image processing (MP4)

AUTHOR INFORMATION

Corresponding Author

Chih-Hao Chang – *Department of Mechanical and Aerospace Engineering, North Carolina State University, Raleigh, North Carolina 27695, United States;* orcid.org/0000-0003-4268-4108; Email: chichang@utexas.edu

Authors

Zhiren Luo – *Department of Mechanical and Aerospace Engineering, North Carolina State University, Raleigh, North Carolina 27695, United States;* orcid.org/0000-0001-6247-0196

Xu A. Zhang – *Department of Mechanical and Aerospace Engineering, North Carolina State University, Raleigh, North Carolina 27695, United States*

Benjamin Aaron Evans – *Department of Physics, Elon University, Elon, North Carolina 27244, United States*

Complete contact information is available at:
https://pubs.acs.org/10.1021/acsami.9b18423

Author Contributions

C.-H.C. conceived of the idea and supervised the study. Z.L. performed the experiments, developed the models, and wrote the manuscript. B.A.E. synthesized the FFPDMS and provided guidance for the magnetic models. X.A.Z. helped with interference lithography and replication process. All of the authors contributed to the paper revision and approved the finalized manuscript.

Notes

The authors declare no competing financial interest.

ACKNOWLEDGMENTS

This work was performed at the NCSU Nanofabrication Facility (NNF) and the Analytical Instrumentation Facility (AIF), members of the North Carolina Research Triangle Nanotechnology Network (RTNN), which is supported by the National Science Foundation as part of the National Nanotechnology Coordinated Infrastructure (NNCI). Z.L., X.A.Z., and C.H.C. were supported by the Defense Advanced Research Projects Agency (DARPA) grant W911NF-15-1-0108 and by National Science Foundation (NSF) grant CMMI#1552424. Contributions from B.A.E. was supported by NSF grant CMMI#1662641.

REFERENCES

(1) Singla, V.; Reiter, J. F. The Primary Cilium as the Cell's Antenna: Signaling at a Sensory Organelle. *Science* **2006**, *313*, 629–633.

(2) Hu, S.; Xia, Z. Rational Design and Nanofabrication of Gecko-Inspired Fibrillar Adhesives. *Small* **2012**, *8*, 2464–2468.

(3) Zhang, S.; Wang, Y.; Onck, P. R.; den Toonder, J. M. J. Removal of Microparticles by Ciliated Surfaces—an Experimental Study. *Adv. Funct. Mater.* **2019**, *29*, 1806434.

(4) Glazer, P. J.; Leuven, J.; An, H.; Lemay, S. G.; Mendes, E. Multi-Stimuli Responsive Hydrogel Cilia. *Adv. Funct. Mater.* **2013**, *23*, 2964–2970.

(5) Drotlef, D.-M.; Blümler, P.; del Campo, A. Magnetically Actuated Patterns for Bioinspired Reversible Adhesion (Dry and Wet). *Adv. Mater.* **2013**, *26*, 775–779.

(6) Cui, J.; Drotlef, D.-M.; Larraza, I.; Fernández-Blázquez, J. P.; Boesel, L. F.; Ohm, C.; Mezger, M.; Zentel, R.; del Campo, A. Bioinspired Actuated Adhesive Patterns of Liquid Crystalline Elastomers. *Adv. Mater.* **2012**, *24*, 4601–4604.

(7) Reddy, S.; Arzt, E.; del Campo, A. Bioinspired Surfaces with Switchable Adhesion. *Adv. Mater.* **2007**, *19*, 3833–3837.

(8) Zarzar, L. D.; Kim, P.; Aizenberg, J. Bio-Inspired Design of Submerged Hydrogel-Actuated Polymer Microstructures Operating in Response to PH. *Adv. Mater.* **2011**, *23*, 1442–1446.

(9) Jager, E. W. H.; Smela, E.; Inganäs, O. Microfabricating Conjugated Polymer Actuators. *Science* **2000**, *290*, 1540–1545.

(10) Evans, B. A.; Shields, A. R.; Carroll, R. L.; Washburn, S.; Falvo, M. R.; Superfine, R. Magnetically Actuated Nanorod Arrays as Biomimetic Cilia. *Nano Lett.* **2007**, *7*, 1428–1434.

(11) Shields, A. R.; Fiser, B. L.; Evans, B. A.; Falvo, M. R.; Washburn, S.; Superfine, R. Biomimetic Cilia Arrays Generate Simultaneous Pumping and Mixing Regimes. *Proc. Natl. Acad. Sci. U.S.A.* **2010**, *107*, 15670–15675.

(12) Sniadecki, N. J.; Anguelouch, A.; Yang, M. T.; Lamb, C. M.; Liu, Z.; Kirschner, S. B.; Liu, Y.; Reich, D. H.; Chen, C. S. Magnetic Microposts as an Approach to Apply Forces to Living Cells. *Proc. Natl. Acad. Sci. U.S.A.* **2007**, *104*, 14553–14558.

(13) Fahrni, F.; Prins, M. W. J.; van IJzendoorn, L. J. Micro-Fluidic Actuation Using Magnetic Artificial Cilia. *Lab Chip* **2009**, *9*, 3413–3421.

(14) Khademolhosseini, F.; Chiao, M. Fabrication and Patterning of Magnetic Polymer Micropillar Structures Using a Dry-Nanoparticle Embedding Technique. *J. Microelectromech. Syst.* **2013**, *22*, 131–139.

(15) Singh, H.; Laibinis, P. E.; Hatton, T. A. Synthesis of Flexible Magnetic Nanowires of Permanently Linked Core–Shell Magnetic Beads Tethered to a Glass Surface Patterned by Microcontact Printing. *Nano Lett.* **2005**, *5*, 2149–2154.

(16) Grigoryev, A.; Tokarev, I.; Kornev, K. G.; Luzinov, I.; Minko, S. Superomniphobic Magnetic Microtextures with Remote Wetting Control. *J. Am. Chem. Soc.* **2012**, *134*, 12916–12919.

(17) Kim, J. H.; Kang, S. M.; Lee, B. J.; Ko, H.; Bae, W.-G.; Suh, K. Y.; Kwak, M. K.; Jeong, H. E. Remote Manipulation of Droplets on a Flexible Magnetically Responsive Film. *Sci. Rep.* **2015**, *5*, 17843.

(18) Cao, M.; Ju, J.; Li, K.; Dou, S.; Liu, K.; Jiang, L. Facile and Large-Scale Fabrication of a Cactus-Inspired Continuous Fog Collector. *Adv. Funct. Mater.* **2014**, *24*, 3235–3240.

(19) Peng, Y.; He, Y.; Yang, S.; Ben, S.; Cao, M.; Li, K.; Liu, K.; Jiang, L. Magnetically Induced Fog Harvesting via Flexible Conical Arrays. *Adv. Funct. Mater.* **2015**, *25*, 5967–5971.

(20) Drotlef, D.-M.; Blümler, P.; Papadopoulos, P.; del Campo, A. Magnetically Actuated Micropatterns for Switchable Wettability. *ACS Appl. Mater. Interfaces* **2014**, *6*, 8702−8707.
(21) Huang, Y.; Stogin, B. B.; Sun, N.; Wang, J.; Yang, S.; Wong, T.-S. A Switchable Cross-Species Liquid Repellent Surface. *Adv. Mater.* **2017**, *29*, 1604641.
(22) Lee, S.-H.; Seong, M.; Kwak, M. K.; Ko, H.; Kang, M.; Park, H. W.; Kang, S. M.; Jeong, H. E. Tunable Multimodal Drop Bouncing Dynamics and Anti-Icing Performance of a Magnetically Responsive Hair Array. *ACS Nano* **2018**, *12*, 10693−10702.
(23) Liu, S.; Long, Y.; Liu, C.; Chen, Z.; Song, K. Bioinspired Adaptive Microplate Arrays for Magnetically Tuned Optics. *Adv. Opt. Mater.* **2017**, *5*, 1601043.
(24) Zhu, Y.; Antao, D. S.; Xiao, R.; Wang, E. N. Real-Time Manipulation with Magnetically Tunable Structures. *Adv. Mater.* **2014**, *26*, 6442−6446.
(25) Luo, Z.; Evans, B. A.; Chang, C.-H. Magnetically Actuated Dynamic Iridescence Inspired by the Neon Tetra. *ACS Nano* **2019**, *13*, 4657−4666.
(26) Chen, C.-M.; Chiang, C.-L.; Yang, S. Programming Tilting Angles in Shape Memory Polymer Janus Pillar Arrays with Unidirectional Wetting against the Tilting Direction. *Langmuir* **2015**, *31*, 9523−9526.
(27) Chen, C.-M.; Yang, S. Directed Water Shedding on High-Aspect-Ratio Shape Memory Polymer Micropillar Arrays. *Adv. Mater.* **2014**, *26*, 1283−1288.
(28) He, X.; Aizenberg, M.; Kuksenok, O.; Zarzar, L. D.; Shastri, A.; Balazs, A. C.; Aizenberg, J. Synthetic Homeostatic Materials with Chemo-Mechano-Chemical Self-Regulation. *Nature* **2012**, *487*, 214−218.
(29) Evans, B. A.; Superfine, R. Design Considerations for Magnetically Actuated Biomimetic Cilia. *Biomimetic Based Applications*; InTech, 2011; pp 473−498.
(30) Zhang, Y.; Lo, C.-W.; Taylor, J. A.; Yang, S. Replica Molding of High-Aspect-Ratio Polymeric Nanopillar Arrays with High Fidelity. *Langmuir* **2006**, *22*, 8595−8601.
(31) Weng, S.; Fu, J. Synergistic Regulation of Cell Function by Matrix Rigidity and Adhesive Pattern. *Biomaterials* **2011**, *32*, 9584−9593.
(32) Smith, H. I. Low Cost Nanolithography with Nanoaccuracy. *Phys. E* **2001**, *11*, 104−109.
(33) Bagal, A.; Chang, C.-H. Fabrication of Subwavelength Periodic Nanostructures Using Liquid Immersion Lloyd's Mirror Interference Lithography. *Opt. Lett.* **2013**, *38*, 2531−2534.
(34) Evans, B. A.; Fiser, B. L.; Prins, W. J.; Rapp, D. J.; Shields, A. R.; Glass, D. R.; Superfine, R. A Highly Tunable Silicone-Based Magnetic Elastomer with Nanoscale Homogeneity. *J. Magn. Magn. Mater.* **2012**, *324*, 501−507.
(35) Yang, R.; Wang, W. A Numerical and Experimental Study on Gap Compensation and Wavelength Selection in UV-Lithography of Ultra-High Aspect Ratio SU-8 Microstructures. *Sens. Actuators, B* **2005**, *110*, 279−288.
(36) Wolfenson, H.; Meacci, G.; Liu, S.; Stachowiak, M. R.; Iskratsch, T.; Ghassemi, S.; Roca-Cusachs, P.; O'Shaughnessy, B.; Hone, J.; Sheetz, M. P. Tropomyosin Controls Sarcomere-like Contractions for Rigidity Sensing and Suppressing Growth on Soft Matrices. *Nat. Cell Biol.* **2016**, *18*, 33−42.
(37) Lohner, J.; Rupprecht, J.-F.; Hu, J.; Mandriota, N.; Saxena, M.; de Araujo, D. P.; Hone, J.; Sahin, O.; Prost, J.; Sheetz, M. P. Large and Reversible Myosin-Dependent Forces in Rigidity Sensing. *Nat. Phys.* **2019**, *15*, 689−695.
(38) Du, P.; Lin, I.-K.; Lu, H.; Zhang, X. Extension of the Beam Theory for Polymer Bio-Transducers with Low Aspect Ratios and Viscoelastic Characteristics. *J. Micromech. Microeng.* **2010**, *20*, 095016.